


Bifurcation diagram and dynamic response of a MEMS resonator with a 1:3 internal resonance

Cite as: Appl. Phys. Lett. **114**, 254104 (2019); <https://doi.org/10.1063/1.5099459>
Submitted: 10 April 2019 . Accepted: 01 June 2019 . Published Online: 25 June 2019

David A. Czaplewski , Scott Strachan, Oriel Shoshani , Steven W. Shaw, and Daniel López 

COLLECTIONS

 This paper was selected as Featured



View Online



Export Citation



CrossMark

ARTICLES YOU MAY BE INTERESTED IN

[A dielectric barrier discharge ion source increases thrust and efficiency of electroaerodynamic propulsion](#)

Applied Physics Letters **114**, 254105 (2019); <https://doi.org/10.1063/1.5100524>

[Segregation particles induced ultrahigh energy storage performances in BiMnO₃ modified BaTiO₃ films](#)

Applied Physics Letters **114**, 253901 (2019); <https://doi.org/10.1063/1.5099926>

[High-gain leaky surface acoustic wave amplifier in epitaxial InGaAs on lithium niobate heterostructure](#)

Applied Physics Letters **114**, 253503 (2019); <https://doi.org/10.1063/1.5108724>

Applied Physics Letters

Mid-IR and THz frequency combs special collection

[Read Now!](#)

AIP
Publishing

Bifurcation diagram and dynamic response of a MEMS resonator with a 1:3 internal resonance

Cite as: Appl. Phys. Lett. **114**, 254104 (2019); doi: [10.1063/1.5099459](https://doi.org/10.1063/1.5099459)

Submitted: 10 April 2019 · Accepted: 1 June 2019 ·

Published Online: 25 June 2019



View Online



Export Citation



CrossMark

David A. Czaplewski,^{1,a)}  Scott Strachan,² Oriel Shoshani,³  Steven W. Shaw,⁴ and Daniel López¹ 

AFFILIATIONS

¹Center for Nanoscale Materials, Argonne National Laboratory, Argonne, Illinois 60439, USA

²Department of Mechanical Engineering and Electrical Engineering, Michigan State University, East Lansing, Michigan 48824, USA

³Department of Mechanical Engineering, Ben-Gurion University of the Negev, Beer-Sheva 84105, Israel

⁴Department of Mechanical and Civil Engineering, Florida Institute of Technology, Melbourne, Florida 32901, USA

^{a)}E-mail: dczaplewski@anl.gov

ABSTRACT

The dynamic response of a nonlinear resonator in the presence of resonant mode coupling is studied experimentally and theoretically. For the case of a clamped-clamped beam resonator in the presence of a 1:3 internal resonance, we show that at the onset of internal resonance, steady state oscillations cannot be sustained. At higher drive levels, stable oscillations can be maintained but the resonator amplitude undergoes amplitude modulated responses. We use these dynamic responses to build a bifurcation diagram that can be described remarkably well with a simple model consisting of a Duffing resonator coupled to a linear one.

Published under license by AIP Publishing. <https://doi.org/10.1063/1.5099459>

Micro- (MEMS) and nanoelectromechanical (NEMS) resonators have found applications in a large variety of fields including force^{1–6} and mass sensing,^{7–11} timing and frequency control,^{12,13} and quantum information science.^{14–16} The majority of these applications rely strongly on operating the resonator in the linear regime for managing their dynamic range, eliminating mixing and modulations, and controlling noise. However, in recent years, there has been considerable interest in effectively capitalizing on the dynamic response of nonlinear resonators to enhance the performance of oscillators. Nonlinear resonators enable mode coupling among vibrational modes, which has been used to greatly improve phase and frequency stability of oscillators,^{17,18} to enhance sensitivity of resonant mass detectors,¹⁹ to control the rate of energy dissipated toward the environment,^{20,21} and to induce parametric amplification in inertial measuring devices.²² In order to allow further optimization and engineering of nonlinear micro- and nanoscale mechanical resonators, a detailed understanding of their dynamic response in the presence of coupled vibrational modes is critically needed.

In this paper, we study the response of a harmonically driven nonlinear MEMS resonator in the presence of resonant mode coupling. The dynamic behavior of a resonator exhibiting a 1:3 internal resonance is used to experimentally build a bifurcation diagram that shows the system dynamics under different operating conditions. We

show that at the onset of internal resonance, steady state oscillations cannot be sustained and the amplitude decays below the noise floor. At higher drive levels, stable oscillations can be maintained but the resonator undergoes modulations in amplitude on slow and fast time scales from modal interactions. Using only device parameters with a single modal coupling coefficient, we present a theoretical analysis of the system that describes the observed dynamic behavior and the bifurcation diagram.

The MEMS resonator used for this research is fabricated from single crystal silicon and is composed of 3 beams, 500 μm long, 3 μm wide, and 10 μm tall, connected at their centers to each other and to a pair of comb drives.¹⁸ The substrate below the device is removed from the backside to prevent levitation of the device during operation. A 6 V DC bias is applied to the resonator. A lock-in amplifier (Zurich Instruments UHFLI) applies a driving voltage to one of the comb drives with an amplitude of V_0 and a driving frequency of f_D . The motion of the resonator creates a motional current in the opposite comb drive that is used to sense its displacement. This current is converted into a voltage through a transimpedance amplifier and then measured using the lock-in amplifier. The linear response of the resonator is characterized by an in-plane flexural motion with $f_{\text{flex}} = 62\,973$ Hz and linear decay rate of $\Gamma_{\text{flex}} = 1.9$ Hz and a higher order, out-of-plane torsional mode with $f_{\text{tor}} = 192\,960$ Hz and $\Gamma_{\text{tor}} = 4.7$ Hz.

For applied drive $V_o > 300 \mu\text{V}$, the flexural mode of the resonator shows nonlinear hardening “Duffing” behavior [Fig. 1(a)]. For a given V_o , as the frequency is swept up, the resonator amplitude increases until a critical frequency is reached (at the saddle node, or SN, bifurcation frequency) where the amplitude abruptly decreases, as seen by the vertical lines in Figs. 1(a) and 1(b). As expected from Duffing behavior,²³ the amplitude and frequency of the SN point increase with increasing drive voltage. From these data, the Duffing coefficient is determined to be $2.47 \times 10^{14} \text{V}^{-2} \text{s}^{-2}$. For driving voltages greater than 17 mV, the SN bifurcation frequencies start to occur at the same drive frequency of $f_{\text{IR}} = 64\,330 \text{ Hz}$, indicating the onset of a 1:3 internal resonance [Fig. 1(b)]. At this frequency, the fundamental flexural mode couples to a high-frequency torsional mode, which occurs at a frequency three times larger than the torsional mode frequency. A detailed description of the phenomena can be found in Refs. 18, 20, and 24.

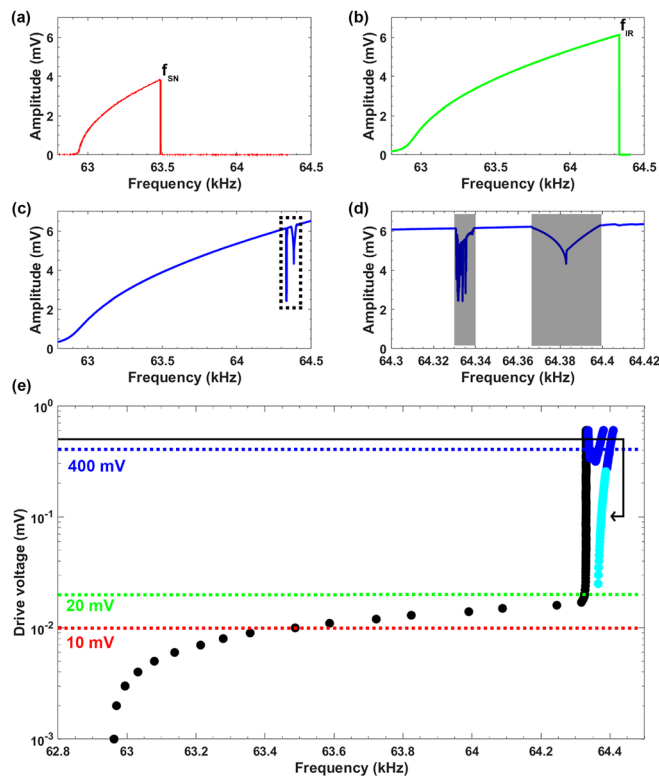


FIG. 1. Dynamic response and bifurcation diagram of a MEMS resonator with 1:3 internal resonance. (a) Voltage response of the resonator for a drive voltage of 10 mV showing a saddle node (SN) bifurcation at f_{SN} . (b) Voltage response of the resonator for a drive voltage of 20 mV showing the onset of internal resonance at f_{IR} . (c) Voltage response of the resonator for a drive voltage of 400 mV. The dotted rectangle indicates the frequency range of interest which is shown in an expanded scale in (d). The shaded regions in (d) indicate the regions where the resonator dynamics deviate from the expected Duffing behavior. (e) Bifurcation diagram of the nonlinear resonator in the presence of resonant mode coupling. The dashed lines correspond to the voltage response data shown in (a)–(c). The light blue data correspond to bifurcation points measured by exciting the resonator through a dynamic path like the one shown by the black arrow.

In order to better visualize the behavior of the resonator as a function of drive voltage, V_o , and driving frequency, f_D , it is helpful to construct a bifurcation diagram with the locus of points where small changes in the system parameters lead to qualitatively different dynamical outcomes [Fig. 1(e)]. The black and blue circles are the frequencies at which the resonator behavior changes, or bifurcates, as the parameters are varied. The dotted color lines in Fig. 1(e) indicate the drive voltage amplitudes corresponding to the frequency responses shown in Figs. 1(a)–1(c), measured by applying a specific V_o and increasing f_D . For example, the response of the resonator with a drive voltage of 10 mV (red line) is seen in Fig. 1(a). The response of the resonator changes at a frequency f_{SN} due to a SN bifurcation, which is plotted as a black circle in Fig. 1(e) on the red dotted line. Similarly, when the resonator is driven at 20 mV (green line), the amplitude increases with increasing frequency until it reaches a frequency f_{IR} [Fig. 1(b)] where the response changes due to the appearance of an internal resonance. This bifurcation frequency is plotted as a black circle in Fig. 1(e) on the green dotted line. At these driving voltages, steady state oscillations cannot be sustained beyond these frequencies. However, for sufficiently large drives, e.g., 400 mV, stable oscillations can be maintained. The response of the resonator can be seen in Fig. 1(c) and shows two different regions at which the behavior deviates from the expected Duffing behavior. The same data are plotted over a smaller frequency window in Fig. 1(d) with the non-Duffing response indicated as gray areas showing where stable oscillations exist as the resonator amplitude undergoes modulations from the modal interactions on a slow time scale (left gray region) and a fast time scale (right gray region). The frequencies limiting these two regions are plotted as black and blue circles in Fig. 1(e).

An interesting feature of these results is that the two regions with nonDuffing dynamics can be observed only after applying a drive voltage beyond a threshold value (260 mV in our case). For drive voltages less than 260 mV, the resonator amplitude drops to the nonresonant linear response (below the noise floor) at the first SN bifurcation and steady state oscillations are not possible beyond this frequency. This limits the ability to characterize the resonator response to frequencies larger than f_{IR} . In order to measure the resonator behavior beyond internal resonance, we follow the response of the system along a dynamic path like the one shown by the black path in Fig. 1(e). A large drive voltage is first applied (500 mV), then the drive frequency is increased well beyond the internal resonance regions, a reduction of the drive voltage to values below 260 mV follows, and subsequently the drive frequency is reduced. As the frequency is reduced, the resonator dynamics follows the expected Duffing behavior before abruptly dropping to the linear response (essentially zero amplitude) at a frequency above f_{IR} . The set of frequencies obtained reducing the frequency are plotted as light blue circles in Fig. 1(e).

The dynamic response of the system can be described by a Hamiltonian with two vibration modes characterized by coordinates q_k and momenta p_k ($k = 1, 2$). The primary mode ($k = 1$) is a flexural mode and is subjected to harmonic drive and shows a quartic Duffing nonlinearity.^{24,25} The secondary mode ($k = 2$) is a torsional mode, which is modeled by a linear harmonic oscillator. The modes are coupled via a nonlinear resonant term that describes the energy exchange between the modes

$$\begin{aligned}
 H &= H_1 + H_2 + H_{int} + H_F, \\
 H_1 &= \frac{1}{2}p_1^2 + \frac{1}{2}\omega_{01}^2q_1^2 + \frac{1}{6}\omega_1q_1^4, & H_2 &= \frac{1}{2}p_2^2 + \frac{1}{2}\omega_{02}^2q_2^2, \\
 H_{int} &= \frac{2}{3}\omega_1\kappa q_1^3q_2, & H_F &= -4\omega_1q_1F \cos(\omega_D t).
 \end{aligned} \quad (1)$$

Dissipative forces are added to each mode, and the complex amplitudes $A_{1,2}$ are used to describe the amplitudes and phases of the modes. The rotating wave approximation is employed to average out fast oscillations, resulting in a pair of equations in (A_1, A_2) that describe their time evolution on a slow scale related to the relaxation time of the modes.¹⁸ These equations are given by

$$\dot{A}_1 = -[1 + i(\Delta\omega_1 - |A_1|^2)]A_1 + i\kappa A_2 \bar{A}_1^2 - iF, \quad (2)$$

$$\dot{A}_2 = -(\Gamma_{21} + i\Delta\omega_2)A_2 + \frac{i\kappa}{9}A_1^3, \quad (3)$$

where $\Delta\omega_1 = 2\pi(f_D - f_{flex})/\Gamma_{flex}$, $\Delta\omega_2 = 2\pi(3f_D - f_{tor})/\Gamma_{flex}$, $\Gamma_{21} = \Gamma_{tor}/\Gamma_{flex}$, κ is the normalized coupling parameter, and F is the normalized driving amplitude, which is proportional to the drive voltage V_o via a calibration factor (for details, see Ref. 24). This model provides a means of predicting the system response as drive parameters (V_o and f_D) are varied for a given set of device parameters. The steady state response (A_{1s}, A_{2s}) of the coupled system can be found by solving $\dot{A}_{1,2} = 0$ which, due to the linearity of the second mode, can be solved for A_{2s} , $[A_{2s} = i\kappa A_{1s}^3/9(\Gamma_{21} + i\Delta\omega_2)]$, which then yields a single implicit expression for A_{1s} in terms of the system and drive parameters

$$F = i \left[1 + i(\Delta\omega_1 - |A_{1s}|^2) + \frac{\kappa^2 |A_{1s}|^4}{9(\Gamma_{21} + i\Delta\omega_2)} \right] A_{1s}. \quad (4)$$

This equation can be used to obtain multivalued frequency response curves for different drive levels.

To assess the stability of the steady state responses and analyze the corresponding bifurcations at the stability thresholds, we employ standard linear stability analysis, by considering the behavior of a small perturbation to the steady state response $(A_{1s} + \delta A_1, A_{2s} + \delta A_2)$. These are substituted into Eqs. (2) and (3) and expanded in terms of the perturbation terms to obtain a linearized system, from which one can determine the eigenvalues that dictate local stability and bifurcations. The attendant characteristic polynomial of the steady response is quartic, of the form $\lambda^4 + c_1\lambda^3 + c_2\lambda^2 + c_3\lambda + c_4 = 0$, where λ are the system eigenvalues and c_i are coefficients that depend on the trace and determinant of the full system Jacobian, \mathbf{J} , which depends, in turn, on the device and drive parameters when evaluated at steady state. In this framework, there are only two generic types of instabilities and attendant bifurcations.²⁶ A SN bifurcation occurs when a real eigenvalue passes through zero, which occurs when $c_4 = 0$. SN bifurcations correspond to the situation in which two response branches merge and annihilate one another as system parameters, in this case V_o or f_D , are varied. The second type is a Hopf bifurcation in which a complex conjugate pair of eigenvalues passes across the imaginary axis as parameters are varied, which occurs when $c_3(c_2c_1 - c_3) - c_4c_1^2 = 0$. At this bifurcation point, there exists a pair of purely imaginary eigenvalues, $\lambda_{1,2} = \pm i\omega_H$, where $\omega_H = \sqrt{c_3/c_1}$ is the frequency of the amplitude modulations near the Hopf

threshold. Hopf bifurcations result in responses that experience periodic modulation of the resonator vibrational amplitude,²⁷ and these can be stable or unstable, depending on parameter conditions. In fact, both types occur in the system model. Several of these bifurcations occur near the internal resonance. A convenient way to display these conditions is by curves in the drive parameter plane (V_o, f_D) that correspond to the SN and Hopf bifurcation conditions.

Figure 2 shows the theoretical values of both SN (red) and Hopf (green) bifurcations, obtained using fitted parameters for the individual modes and a single modal coupling coefficient ($\tilde{\kappa} = 2.964 \times 10^{12} \text{ V}^{-2} \text{ s}^{-2}$), overlaid with the experimental data. A plot over a smaller frequency range [Fig. 2(b)] shows the structure near the IR more clearly and shows remarkable agreement with the experimental data. Additionally, the model predicts bifurcations that are not experimentally accessible (red values occurring slightly higher in frequency than the IR). The IR causes a saturation of the SN bifurcations at a frequency nearly one third of the torsional mode. The bifurcation conditions provide an excellent estimation of the regions of parameter space where the Duffing response is observed. One interesting result of this internal resonance is the creation of a gap in the system parameters where stable oscillations cannot be sustained. For driving frequencies between the SN bifurcations on the left (black circles) and the Hopf

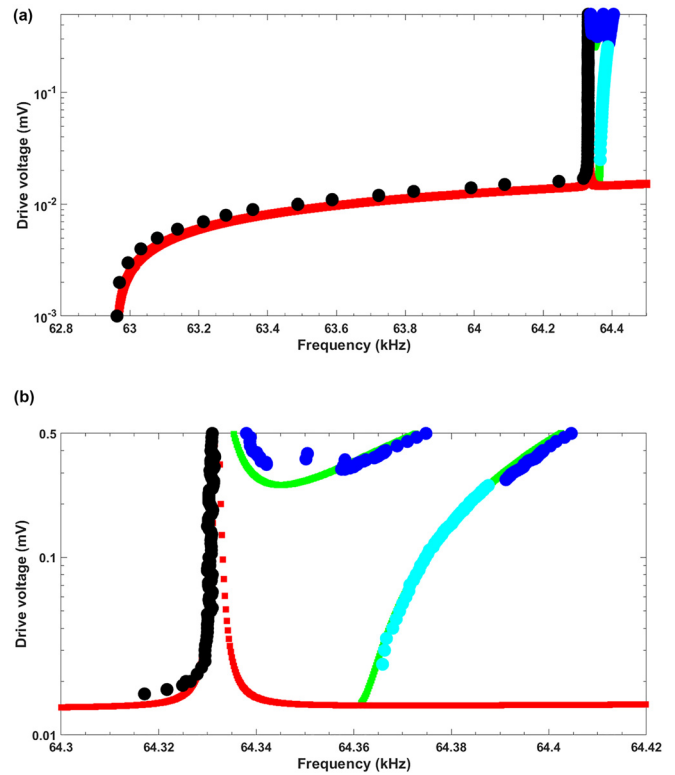


FIG. 2. Comparison of experimental and theoretical bifurcation diagrams. (a) Extended diagram showing the good agreement between model and experiment. The red line is the predicted location of the saddle node bifurcation using system parameters as a fitting variable. The area in the vicinity of the internal resonance is shown in detail in (b). (b) The solid lines indicate the system bifurcations as described by Eq. (1): SN bifurcation (red line) and Hopf bifurcation (green line). The solid circles indicate the experimental data from Fig. 1(e).

bifurcations on the right (light blue circles) and below a threshold driving voltage of 260 mV, the resonator's amplitude will decay to zero. This gap in the operating parameter space is created by the presence of a mode coupling in the resonator: the higher frequency mode drains mechanical energy from the first mode reducing its amplitude to the point where oscillations at that frequency are unstable, thus causing the amplitude to drop to the lower branch of the resonant curve. Our results indicate that mode coupling is most easily achieved when the dissipation in the resonator is small or, conversely, when the quality factor, Q , of the resonator is high. Therefore, applications using high Q resonators need to be aware of coupling with higher order modes to avoid accidentally creating such voids in the operating regime.

In summary, we have studied the dynamic response of a MEMS resonator with Duffing nonlinear behavior that has a 1:3 internal resonance. The dynamic responses at internal resonance consist of a region of operating parameters where the resonator does not have stable vibrations and regions where it experiences amplitude modulated oscillations. The experimental observations are used to create a bifurcation diagram that can be precisely described with a standard 1:3 internal resonance model incorporating measured modal parameters and a fitted coupling strength. In a future study, we plan to investigate noise-induced phenomena, such as stochastic switching and stochastic resonance in the vicinity of the 1:3 internal resonance conditions.

The authors would like to acknowledge Mark Dykman for helpful discussion regarding both the theoretical and experimental results. This work was performed, in part, at the Center for Nanoscale Materials, a U.S. Department of Energy Office of Science User Facility, and supported by the U.S. Department of Energy, Office of Science, under Contract No. DE-AC02-06CH11357. O.S. acknowledges partial support from the Ben-Gurion University of the Negev. S.W.S. acknowledges support for this work from the U.S. National Science Foundation under Grant Nos. CMMI-1662619 and CMMI-1561829.

REFERENCES

- ¹D. Rugar, R. Budakian, H. Mamin, and B. Chui, *Nature* **430**, 329 (2004).
- ²E. Gavartin, P. Verlot, and T. J. Kippenberg, *Nat. Nanotechnol.* **7**, 509 (2012).
- ³J. Moser, J. Güttinger, A. Eichler, M. J. Esplandiu, D. Liu, M. Dykman, and A. Bachtold, *Nat. Nanotechnol.* **8**, 493 (2013).
- ⁴M. S. Hanay, S. I. Kelber, C. D. O'Connell, P. Mulvaney, J. E. Sader, and M. L. Roukes, *Nat. Nanotechnol.* **10**, 339 (2015).
- ⁵R. Decca, D. Lopez, E. Fischbach, and D. Krause, *Phys. Rev. Lett.* **91**, 050402 (2003).
- ⁶D. Lopez, R. Decca, E. Fischbach, and D. Krause, *Bell Labs Tech. J.* **10**, 61 (2005).
- ⁷K. Jensen, K. Kim, and A. Zettl, *Nat. Nanotechnol.* **3**, 533 (2008).
- ⁸J. Lee, W. Shen, K. Payer, T. P. Burg, and S. R. Manalis, *Nano Lett.* **10**, 2537 (2010).
- ⁹E. Gil-Santos, D. Ramos, J. Martínez, M. Fernández-Regúlez, R. García, Á. San Paulo, M. Calleja, and J. Tamayo, *Nat. Nanotechnol.* **5**, 641 (2010).
- ¹⁰J. Chaste, A. Eichler, J. Moser, G. Ceballos, R. Rurali, and A. Bachtold, *Nat. Nanotechnol.* **7**, 301 (2012).
- ¹¹V. Puller, B. Lounis, and F. Pistolesi, *Phys. Rev. Lett.* **110**, 125501 (2013).
- ¹²C. Lam, in *2008 IEEE Ultrasonics Symposium, IUS 2008* (IEEE, 2008), pp. 694–704.
- ¹³J. Van Beek and R. Puers, *J. Micromech. Microeng.* **22**, 013001 (2012).
- ¹⁴S. Kolkowitz, A. C. B. Jayich, Q. P. Unterreithmeier, S. D. Bennett, P. Rabl, J. Harris, and M. D. Lukin, *Science* **335**, 1603 (2012).
- ¹⁵T. Palomaki, J. Teufel, R. Simmonds, and K. Lehnert, *Science* **342**, 710 (2013).
- ¹⁶E. Verhagen, S. Deléglise, S. Weis, A. Schliesser, and T. J. Kippenberg, *Nature* **482**, 63 (2012).
- ¹⁷L. Villanueva, E. Kenig, R. Karabalin, M. Matheny, R. Lifshitz, M. Cross, and M. Roukes, *Phys. Rev. Lett.* **110**, 177208 (2013).
- ¹⁸D. Antonio, D. H. Zanette, and D. López, *Nat. Commun.* **3**, 806 (2012).
- ¹⁹T. Zhang, X. Wei, Z. Jiang, and T. Cui, *Appl. Phys. Lett.* **113**, 223505 (2018).
- ²⁰C. Chen, D. H. Zanette, D. A. Czapslewski, S. Shaw, and D. López, *Nat. Commun.* **8**, 15523 (2017).
- ²¹J. Güttinger, A. Noury, P. Weber, A. M. Eriksson, C. Lagoin, J. Moser, C. Eichler, A. Wallraff, A. Isacsson, and A. Bachtold, *Nat. Nanotechnol.* **12**, 631 (2017).
- ²²S. Nitzan, V. Zega, M. Li, C. Ahn, A. Corigliano, T. Kenny, and D. Horsley, *Sci. Rep.* **5**, 9036 (2015).
- ²³A. H. Nayfeh, *Nonlinear Interactions: Analytical, Computational and Experimental Methods* (Wiley, 2000).
- ²⁴D. A. Czapslewski, C. Chen, D. Lopez, O. Shoshani, A. M. Eriksson, S. Strachan, and S. W. Shaw, *Phys. Rev. Lett.* **121**, 244302 (2018).
- ²⁵F. Mangussi and D. Zanette, *PLoS One* **11**, e0162365 (2016).
- ²⁶P. R. Sethna and A. K. Bajaj, *J. Appl. Mech.* **45**, 895 (1978).
- ²⁷S. Hourli, D. Hatanaka, M. Asano, R. Ohta, and H. Yamaguchi, *Appl. Phys. Lett.* **114**, 103103 (2019).